INTERNATIONAL JOURNAL OF HYDROGEN ENERGY 43 (2018) 6838–6850

Available online at www.sciencedirect.com

ScienceDirect

journal homepage: www.elsevier.com/locate/he

The effect of TiO_2 nanotube morphological engineering and ZnS quantum dots on the water splitting reaction: A theoretical and experimental study

M.A. Santanna [a], W.T. Menezes [b], Y.V.B. Santana [a,c], M.M. Ferrer [d], A.F. Gouveia [a], A.D. Faceto [e], A.J. Terezo [b], A.J.A. Oliveira [e], E. Longo [a,f], R.G. Freitas [b,*], E.C. Pereira [a]

[a] Department of Chemistry, Federal University of São Carlos, Laboratório Interdisciplinar de Eletroquímica e Cerâmia, P.O. Box 676, 13565-905, São Carlos, SP, Brazil

[b] Department of Chemistry, Federal University of Mato Grosso, Laboratório Computacional de Materiais and Grupo de Eletroquímica e Novos Materiais, 78060-900, Cuiabá, MT, Brazil

[c] Federal Technological University of Paraná, 86300-000, Cornélio Procópio, PR, Brazil

[d] Modeling and Molecular Simulations Group, São Paulo State University, UNESP, 17033-360, Bauru, SP, Brazil

[e] Department of Physics, Federal University of São Carlos, P.O. Box 676, 13565-905, São Carlos, SP, Brazil

[f] Sao Paulo State University, UNESP, 14800-900, Araraquara, SP, Brazil

ARTICLE INFO

Article history:
Received 11 November 2017
Received in revised form
14 February 2018
Accepted 17 February 2018
Available online 13 March 2018

Keywords:
TiO_2 nanotubes
Morphology control
Water splitting
Rietveld refinement
Materials modelling

ABSTRACT

Ordered arrays of TiO_2 nanotubes with smooth and rippled morphologies were prepared by one-step titanium oxidation in NH_4F and ethylene glycol solution. The samples were then decorated with ZnS using a microwave-assisted solvothermal method. The experiments under constant or pulsed applied voltage resulted in smooth and rippled TiO_2material morphologies, respectively. Field emission scanning electron microscopy, incident photon-to-current efficiency, linear sweep voltammetry and electrochemical impedance spectroscopy were used to investigate the structure and morphology of the TiO_2 nanotubes, along with their photoelectrochemical activity in the water splitting reaction. An envelope function was proposed to correlate the anisotropic morphologies and broad distribution of mobility due to the random nature of charge carrier transport. The smooth and rippled morphologies were evaluated using the transmission line model. First-principles quantum mechanical calculations based on the density functional theory at the B3LYP level are conducted to obtain a better understanding of optical properties of TiO_2.

Introduction

The annual power consumption of the global population (nearly 7 billion people) is greater than 15TW [1]. By contrast, to address such power needs using sunlight, the earth area to be covered would only be about 0.19% of the surface (900,000 km^2) with typically 10% efficiency solar cells. Therefore, sunlight offers a huge potential for a global supply of

* Corresponding author.
E-mail address: rgfreitas@ufmt.br (R.G. Freitas).
https://doi.org/10.1016/j.ijhydene.2018.02.113

clean, renewable energy. Thus, the design of semiconductor materials able to convert solar energy into electrical power is an important target.

In this context, one-dimensional nanostructures of TiO_2, such as TiO_2 nanotubes (TiO_2NT) seem to be one of the most promising energy harvesting materials due to their chemical stability, narrow band gap and appropriate band edge positions for the water splitting application. A number of factors affect the properties of electrochemically synthesized TiO_2NT. Schmuki et al. [2] conducted a comprehensive study on Ti foil anodization, and concluded that different parameters, e.g. the electrolyte, F^- precursor species, applied voltage, time and temperature control TiO_2NT morphology. Among these factors, one of the most important variables is the waveform of the applied voltage [2]. In the same work, the authors [2] suggested that using a constant applied voltage results in smooth nanotube morphology. Conversely, in a different study, Schmuki et al. [3] used pulsed applied voltage anodization (120–40 V) to obtain a bamboo-like morphology. Samia et al. [4] studied these bamboo-like nanotubes and their performance in a dye-sensitized solar cell (DSSC). According to the authors [4], a higher density of bands along the bamboo-like nanotubes enhanced the efficiency up to 3.46% compared to 2.0% obtained for smooth nanotubes. Takahashi et al. [5] studied the photoelectrochemical water splitting reaction over rippled and smooth TiO_2NT morphologies prepared using two-step anodization. According to the authors [5], in contrast to the proposition of Samia et al. [4] the incident photon-to-current conversion efficiency (IPCE) increased up to 300% with the smooth sample compared to rippled TiO_2NTs. Therefore, it seems that the photoelectrochemical response of these systems is complex depending on different factors.

Electrochemical impedance spectroscopy (IS) is a powerful technique to study interfacial phenomena, such as the effect of smooth and rippled TiO_2NTs on charge transfer over an interface. To the best of our knowledge, only Bisquert et al. [6] have studied the interfacial phenomena of smooth TiO_2NT using a transmission line model (TL) [7,8]. However, the system chosen was a DSSC. Therefore, there have been no studies providing a systematic assessment of the effect of TiO_2NT morphology on the water-splitting reaction using the TL model.

As described above, TiO_2NT morphology can influence the photoelectrochemical properties [4,5]. Furthermore, TiO_2NTs associated with semiconductor quantum dots (QDs) such as ZnS [9] have many potential advantages, including high stability [10], light absorption in the visible region [10], tunable band gaps [11], a high molar extinction coefficient [12] and a large intrinsic dipole moment enhancing charge separation [13]. Under illumination, QDs absorb light and inject electrons into the TiO_2 conduction band [9], while holes are removed by the reductant in the electrolyte and further regenerated at the counter electrode.

Considering the above, here we report the preparation of vertically oriented TiO_2NT photoelectrodes with a smooth or rippled morphology associated with ZnS quantum dots. The TiO_2NT photoelectrodes were characterized by FE-SEM and the photoelectrochemical activity in the water splitting reaction was evaluated using the IPCE and linear sweep voltammetry (LSV) techniques. An envelope function was proposed to correlate the anisotropic morphologies and broad distribution of mobility due to the random nature of charge carrier transport. The effects of the sample's morphology in the water splitting reaction were described using IS and TL modelling. In order to explain some experimental outcomes of TiO_2NT, quantum mechanical results were calculated based on density functional theory (DFT) at the B3LYP level. The electronic band structure, density of states (DOS) and the charge map of TiO_2 have been shown in order to better evaluate the relation of structural and electronic properties.

Experimental

Electrode preparation

TiO_2NT arrays were prepared by anodizing 1.0 cm^2 of titanium foil (99.8% Alfa Aesar) in electrolytes composed of ethylene glycol (Synth), Milli-Q water (10 vol%), and NH_4F (Sigma Aldrich) (0.25 wt%). Prior to each anodization, Ti samples were ultrasonicated in acetone followed by a distilled water rinse and dried in an N_2 stream. Anodization was performed at 25 °C using a standard two-electrode cell with the Ti foil as the anode and platinum foil (4.0 cm^2) as the cathode using a Keithley-2410 sourcemeter. Two different samples were prepared: the TiO_2NT-CV sample was prepared by sweeping the voltage from the open circuit potential up to 40 V at 0.1 Vs^{-1} and maintaining the applied voltage at its end value for 120 min. The TiO_2NT-PV sample was synthesized by sweeping the voltage from the open circuit potential at 0.1 Vs^{-1} up to 40 V, and then the voltage was pulsed between 40 V and 20 V, every 10 min for 12 cycles. After the anodization process, the samples were rinsed with distilled water and thermally treated at 450 °C for 120 min to eliminate water and the organic portion, to improve its mechanical stability and to obtain the TiO_2-anatase phase. A cooling rate of 5.0 °C min^{-1} was used.

The microwave-assisted solvothermal (MAS) method was used to obtain ZnS quantum dots along the TiO_2NT surface. The ZnS precursor solution was obtained as described by Longo et al. [14] In the sequence, the solution was transferred into a Teflon autoclave, and the TiO_2NT-CV or TiO_2NT-PV samples were placed inside. The vessel was sealed and placed inside a domestic microwave-solvothermal system (2.45 GHz, maximum power of 800 W). MAS processing was performed at 140 °C for 16 min. To remove any byproducts, the resulting TiO_2NT/ZnS material was washed with deionized water and ethanol several times, and finally dried in an N_2 stream. The electrodes were designated TiO_2NT/ZnS_{QD}-CV and TiO_2NT/ZnS_{QD}-PV for those obtained with constant or pulsed voltage, respectively.

Electrode characterization

The X-ray diffraction (XRD) patterns were obtained using a Siemens diffractometer model D-5000 with Cu Kα radiation and $\lambda = 1.5406$ Å. To obtain the microstructural data of the TiO_2NT electrodes, a Rietveld refinement [15] was performed using the General Structure Analysis System (GSAS) program suite [16] with the EXPGUI interface [17].

Morphological characterization was carried out using a Supra 35 Zeiss field emission scanning electron microscope. UV–Vis spectra were taken using a Varian spectrophotometer (model Cary 5G) in a diffuse-reflectance mode. The electrochemical measurements were performed using an Autolab PGSTAT-30 potentiostat/galvanostat. All electrochemical water-splitting measurements were performed in a three-electrode configuration using Ag/AgCl in saturated KCl as the reference electrode, a counter electrode of platinum wire and a TiO_2NT electrode as the photoanode. The measurements were performed in 0.5 M Na_2SO_4 media and illuminated with a Xenon lamp using a Newport Oriel Instrument 66881 QTH model. All experiments were conducted at 25 °C.

IS was measured with an excitation signal of 5.0 mV in the frequency range from 10 KHz to 10 mHz. Before each experiment, the electrodes were polarized at 0.2 V for 5 min to reach the steady state. The impedance data were analyzed using the TL model, which is, as proposed by Bisquert et al. [7,8] adequate to analyze tubular material structures and the relationship between nanotubes and the solution inside the tubes.

Theoretical calculation

The electronic structure calculations for TiO_2 models were performed using a periodic approximation implemented in the CRYSTAL09 computer code [18]. The computational method is based on DFTin conjunction with Becke's three-parameter hybrid non-local exchange functional [19] combined with the Lee–Yang–Parr gradient-corrected correlation functional, B3LYP [20]. Ti and O atomic centers are described by basis sets 86-411d4-1 and 6-31d1 which were taken from the Mike Towler's Crystal web site [21] and Crystal web site [22], respectively. The diagonalization of the Fock matrix was performed at adequate *k*-point grids in the reciprocal space, which is the Pack-Monkhorst/Gilat shrinking factor IS = ISP = 6. Thresholds controlling the accuracy of the Coulomb and exchange integral calculations were set to 10^{-7} (ITOL1 to ITOL4) and 10^{-14} (ITOL5) which assures a convergence in total energy better than 10^{-7}a.u. whereas the percentage of the Fock/Kohn–Sham matrix mixing was set to 90 (IPMIX = 90) [18]. Full optimization of (*a*, *b*, *c*) lattice parameters as well as (*x*, *y*, *z*) internal coordinates was conducted. The band structure diagram and DOS were carried out with CRYSTAL09, and the charge maps with XCRYSDEN [23]. Three models were constructed to more accurately describe structural and electronic properties derived from the experimental synthesis, an ordered bulk (o-TiO_2), disordered bulk (d-TiO_2) with displacement of O atom in lattice, and nanotube model (TiO_2NT).

Results and discussion

Theoretical calculations and computer simulations can complement experimental methods and have revealed new insights into medium-range order and dynamic changes in local structure [24]. To understand the relationship between the morphology and the structural disorder in complex clusters, with an intermediate-range interaction (interaction between two clusters) and the resulting electronic defects that are generated, a detailed theoretical study was made for three TiO_2 periodic models. A TiO_2 ordered bulk (o-TiO_2), disordered TiO_2 bulk (d-TiO_2) and TiO_2 nanotube (TiO_2NT) were represented in Fig. 1.

Regarding the simulations results, Fig. 2 represents the band structure of the bulk o-TiO_2, d-TiO_2 and TiO_2NT. For the o-TiO_2 and d-TiO_2 models the top of the valence band is located at X point and both presented indirect band gap (X - Γ points) with 3.69 eV and 3.09 eV respectively. For the nanotube simulation the band gap is also indirect transition between N - Γ transition points and the band gap value presents a significant drop to 2.49 eV being in agreement with the experimental values. It is possible to observe an expressive decrease in the band gap values observed in the d-TiO_2 and TiO_2NT models. These results are derivate from the creation of the new intermediated levels in the prohibited zone between the valence and conduction bands. This fact occurs because in theses models the [TiO_6] clusters that constituted the structure are distorted and theses distortions can be in function of the bond distances, bond angles and dihedral angles that constitute the defects of short, medium and long distances, respectively. All these defects are responsible by the electronic levels modifications in different way, resulting in changes in the band gap.

The UV–Visible diffuse reflectance spectra of TiO_2NT were recorded (S1) and the optical band gap energy was calculated using the method proposed by Wood e Tauc [25]. The values obtained were 2.65 eV, 2.82 eV, 2.40 eV and 3.00 eV for TiO_2NT-CV, TiO_2NT-PV, TiO_2NT/ZnS_{QD}-CV and TiO_2NT/ZnS_{QD}-PV respectively. Therefore, compared to TiO_2NT simulation, it was observed an agreement between theoretical and experimental values close to 5.0%.

An analysis of the projected density of state (DOS) is presented in Fig. 3. It is possible verify that the valence band is composed mainly by "O" orbitals while the conduction band by "Ti" orbitals for all models. The difference observed in DOS profiles and band gap between the bulk ordered and disordered (o-TiO_2 and d-TiO_2) and the nanotube model occurs due to the change of bond characteristics, such as angles, and because of the exposed surface found in the last model. So, the defects in the lattice are directly related with the electronic properties since was observed the decrease in the band gap values for d-TiO_2.

Fig. 4 shows the charge map of all models in order to evaluate the differences due to the bond characteristics. The defect created in the bulk system can be observed by comparing the o-TiO_2 with d-TiO_2 (Fig. 4a and b). In this case, the displacement of "O" atom, distanced from "Ti", caused a polarization in the system. It is possible to notice that the density of charge it is not equally distributed in the "Ti" and "Ti" atoms in the defect region (Fig. 4b). This defect can be attributed to distortions of the bond distances, bond angles and dihedral angles that constitute the defects of short, medium and long distances, respectively. How explained in the band gap analysis, these defects are responsible by the electronic levels modifications. Besides that, Fig. 4c shows the expressive difference of TiO_2-NT system of a plane of the inner part of the nanotube where the charge distributions are

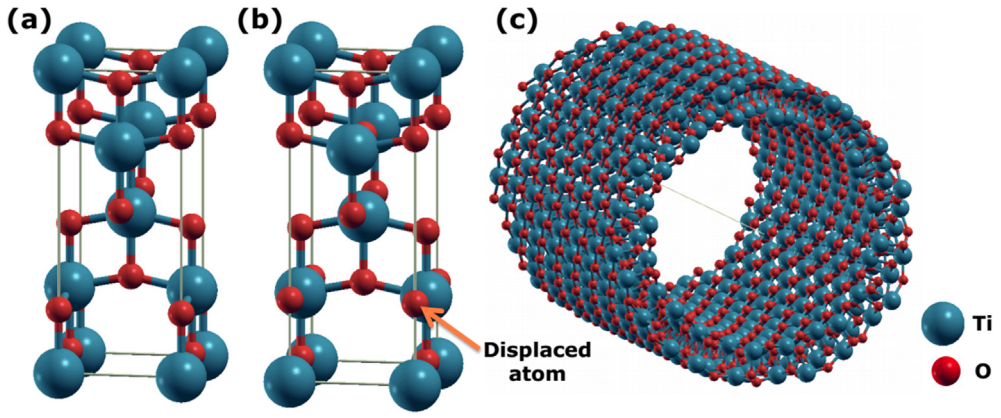

Fig. 1 – Structural schemes used in theoretical calculations for: a) o-TiO_2, b) d-TiO_2 and c) NT-TiO_2 models.

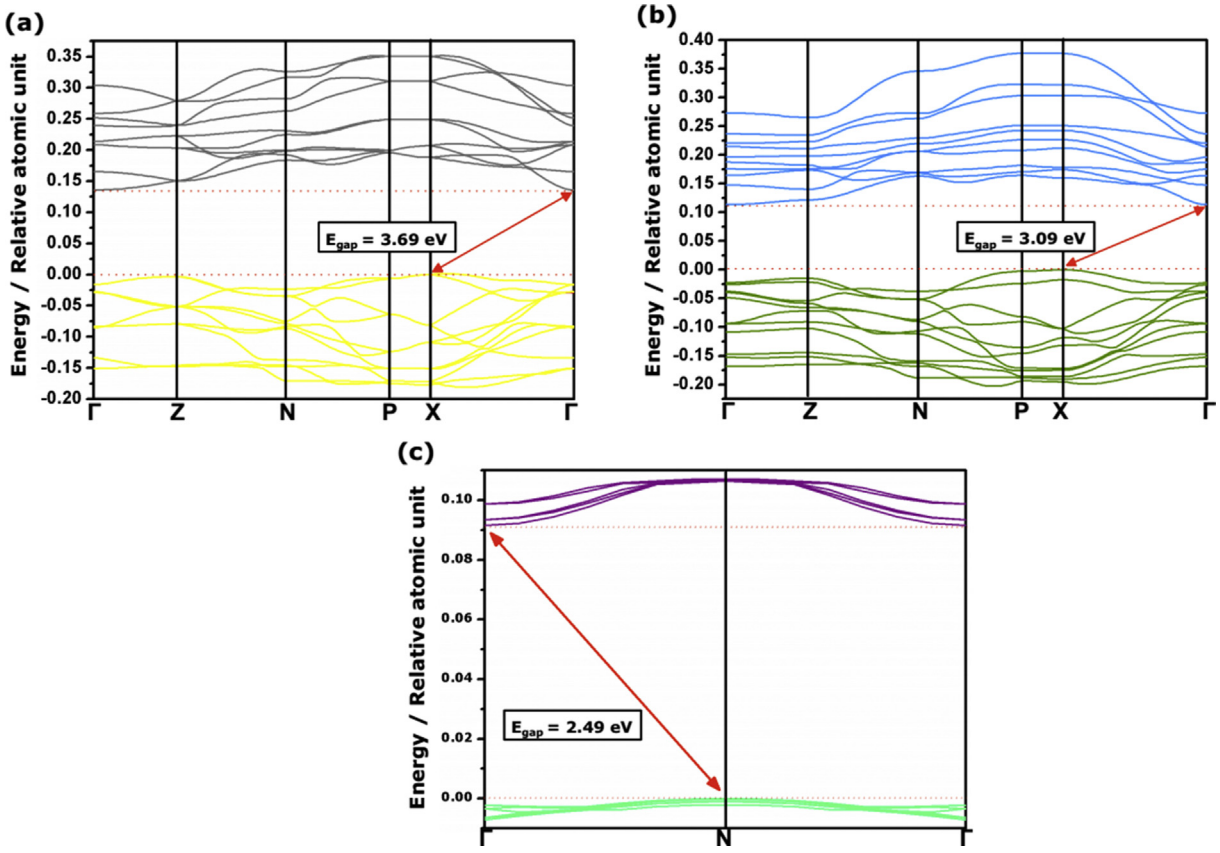

Fig. 2 – Band structures and band gap values of: a) o-TiO_2, b) d-TiO_2 and c) NT-TiO_2.

not uniform between the atoms. This is evidence that there is presence of local defects in the NT-TiO_2 structure further the fact of the lower bang gap value. Therefore, it is important to emphasize that the presence of defects and, consequently, the lower of the band gap value facilitate the split of the pair electron-hole (e^-/h^+) and the material becomes more reactive.

Besides, from these theoretical results it is possible to conclude that the nanotube structure is the most promising morphology towards energy conversion. Therefore, this morphology was chosen as starting point for further modification and experimental engineering over TiO_2 structure.

The current versus time curves obtained during the anodization of TiO_2NT under constant and pulsed voltage are shown in Fig. 5. It is possible to observe a sharp drop in current due to the formation of the barrier layer, followed by an increase of the current caused by pitting of the oxide layer by fluoride ions. In Fig. 5a, it is possible to observe that the current reached a steady value. Such behavior was not observed in Fig. 5b since pulsed voltage anodization was applied.

According to Schmuki et al. [2], the most important factor controlling the diameter of the tube is the anodization voltage. These authors [2] observed that the size of the tube diameter

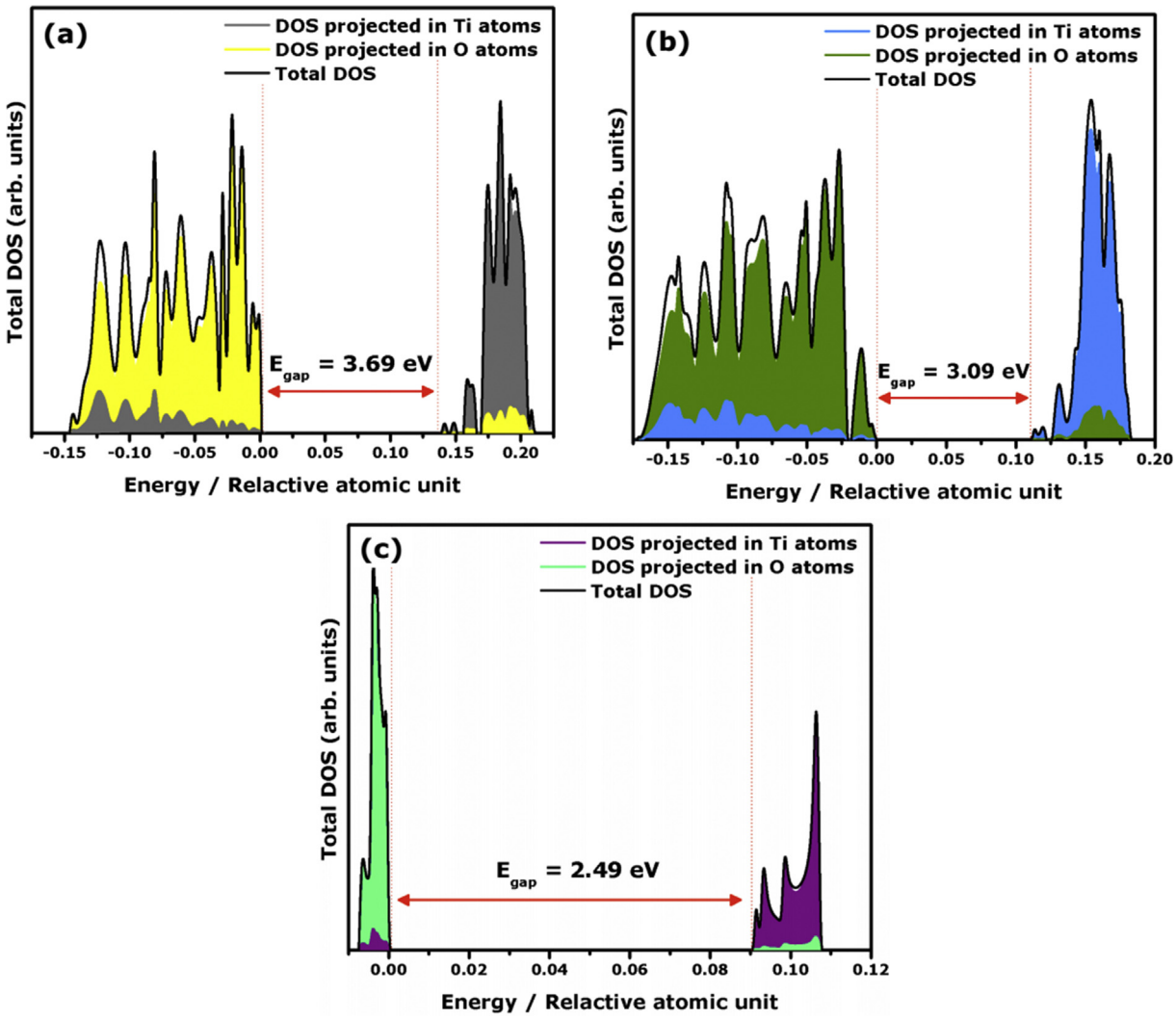

Fig. 3 – Density of states projected in Ti and O atoms for: a) o-TiO_2, b) d-TiO_2 and c) NT-TiO_2.

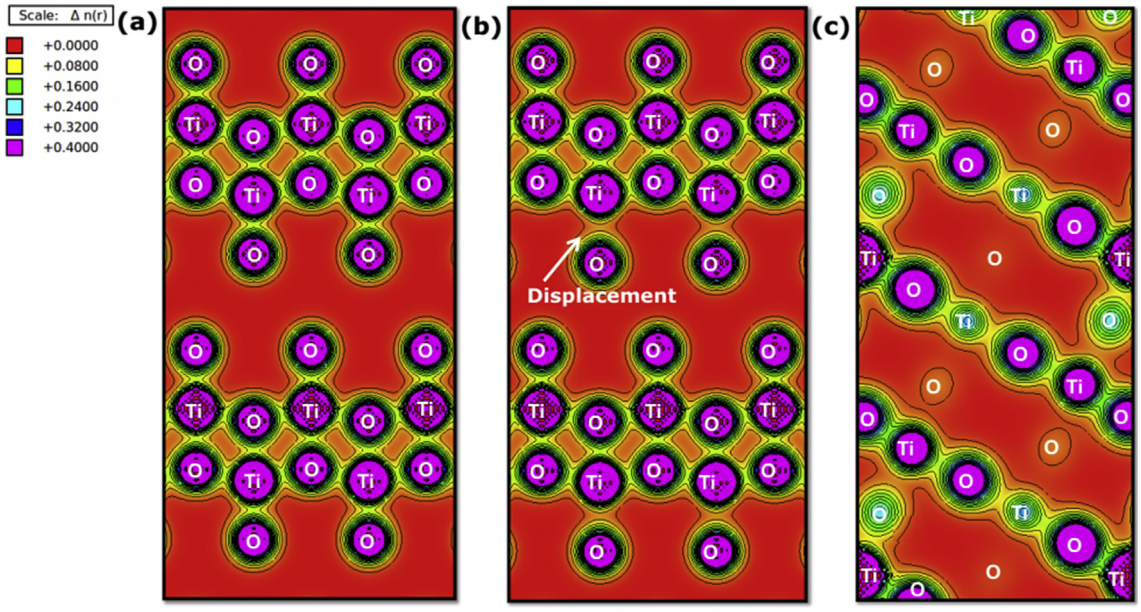

Fig. 4 – Charge density map of: a) o-TiO_2, b) d-TiO_2 and c) NT-TiO_2.

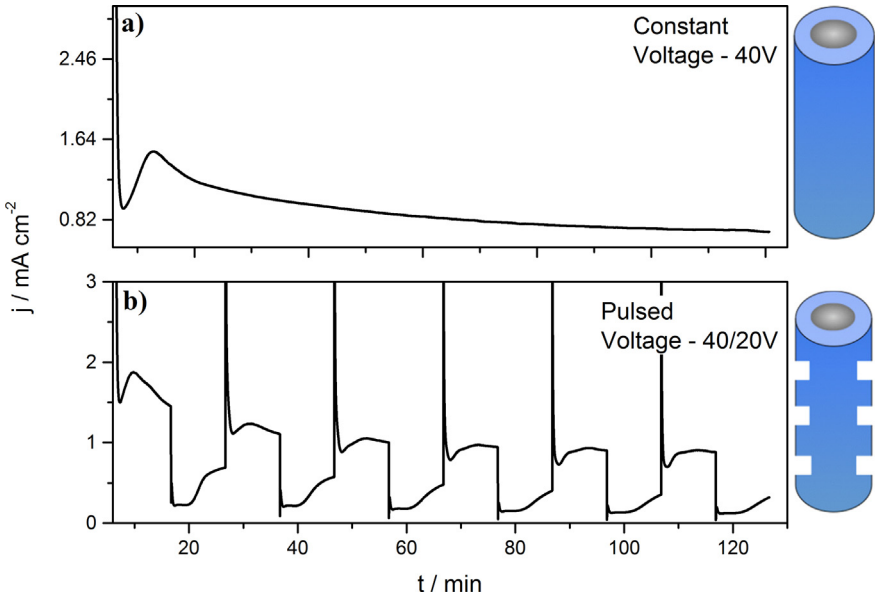

Fig. 5 – Constant and pulsed chronoamperograms for TiO_2NT anodization in ethylene glycol + water (10 vol %) + NH_4F (0.25 wt %). T = 25 °C. a) $E_{Const.}$ = 40 V and b) E_{Pulsed} = 40–20 V.

depends on the applied voltage; therefore, it should be expected that constant and pulsed voltage results in smooth and rippled morphologies, as pictorially represented in Fig. 5a and b (on the right side). The FE-SEM images of TiO_2NT prepared under constant or pulsed voltage with or without ZnS QD decoration are shown in Fig. 6a–d, respectively.

It is possible to identify a smooth morphology for TiO_2NT-CV and TiO_2NT/ZnS_{QD}-CV prepared under constant voltage in Fig. 6a and c respectively. Otherwise, for TiO_2NT-PV and TiO_2NT/ZnS_{QD}-PV, it is possible to observe several layers related to step voltage (40–20 V), as indicated by arrows in Fig. 6b and d, respectively. As the thickness of each layer was close to 400 nm and the pulsed voltage step was 12 min, the TiO_2NT growth rate was almost 33.3 nm min^{-1}. For comparison, Schmuki et al. [26] observed a growth rate up to 40 nm min^{-1}, which depends on the applied voltage as well the water and fluoride concentrations.

The Rietveld refinement data obtained for TiO_2NT-CV, TiO_2NT-PV, TiO_2NT/ZnS_{QD}-CV and TiO_2NT/ZnS_{QD}-PV are shown in Figure S2 along the supplementary information section. The quality of the structural refinement data is acceptable when the weighted index (R_{wp}) is $R_{wp} < 10\%$ [16] and the discrepancy between the observed values and the values expected under the model in question (χ^2) is lower than two [16]. Therefore, it was possible to observe that the Rietveld refinement evaluated for the photoelectrodes was in agreement with the Rietveld procedure.

All samples presented TiO_2-Anatase phase with tetragonal structure in accordance with the JCPDS card PDF n° 2022-42. Table 1 presents the parameters obtained by the Rietveld refinement for all samples, which will be further used as input to perform DFT calculus and obtain electronic properties. No significant differences on the unit cell could be observed by the refinement simulations, neither the presence of ZnS structure could be detected on samples TiO_2NT/ZnS_{QD}-CV and TiO_2NT/ZnS_{QD}-PV.

Since it was not possible to observe the ZnS phase on the XRD, EDX analysis were performed on decorated nanotubes to verify the presence of Zn and S elements (S3). Despite of the small concentrations of Zn and S found, these results indicate the achievement of the decoration.

In order to investigate the photoresponse of TiO_2NT photoelectrodes, *i*-V curve profiles under Xenon lamp were also carried out by linear sweep voltammetry, as shown in Fig. 7. The LSV for one of the samples is also presented under dark conditions, in order to measure any leakage current.

The photocurrent density for all sets of samples increased as the applied potential was displaced towards positive values, reaching a plateau at 0.1 V. It is also possible to observe an increase in the peak photocurrent for TiO_2NT/ZnS_{QD}-CV of 80% compared to the TiO_2NT/ZnS_{QD}-PV sample. Finally, for those materials synthesized using constant voltage anodization, greater water splitting photoactivity was observed compared to the TiO_2NT-PV samples. One possible explanation could be, as described previously, that the anisotropic morphologies are prone to exhibiting charge-trapping sites with both shallow and deep traps.

To investigate this hypothesis, IS measurements were performed for all samples; the results are presented in Fig. 8. In the literature, IS has been used to evaluate changes in TiO_2NT morphologies by analyzing the results using equivalent circuits [27,28]. However, according to the model proposed by de Levie [29–31], a more detailed description of semi-infinite and finite-length cylindrical diffusion species in a porous electrode must be taken into account, which can be conveniently described using a TL model. Bisquert et al. developed a comprehensive series of TL models for organic [8] and inorganic [6,32] nanostructured systems.

According to Bisquert et al. [6], for vertically oriented TiO_2NTs of length (*L*) immersed in an electrolyte, it is expected to find typical impedance behavior of the porous electrode described by the TL model shown in Fig. 8a [33,34].

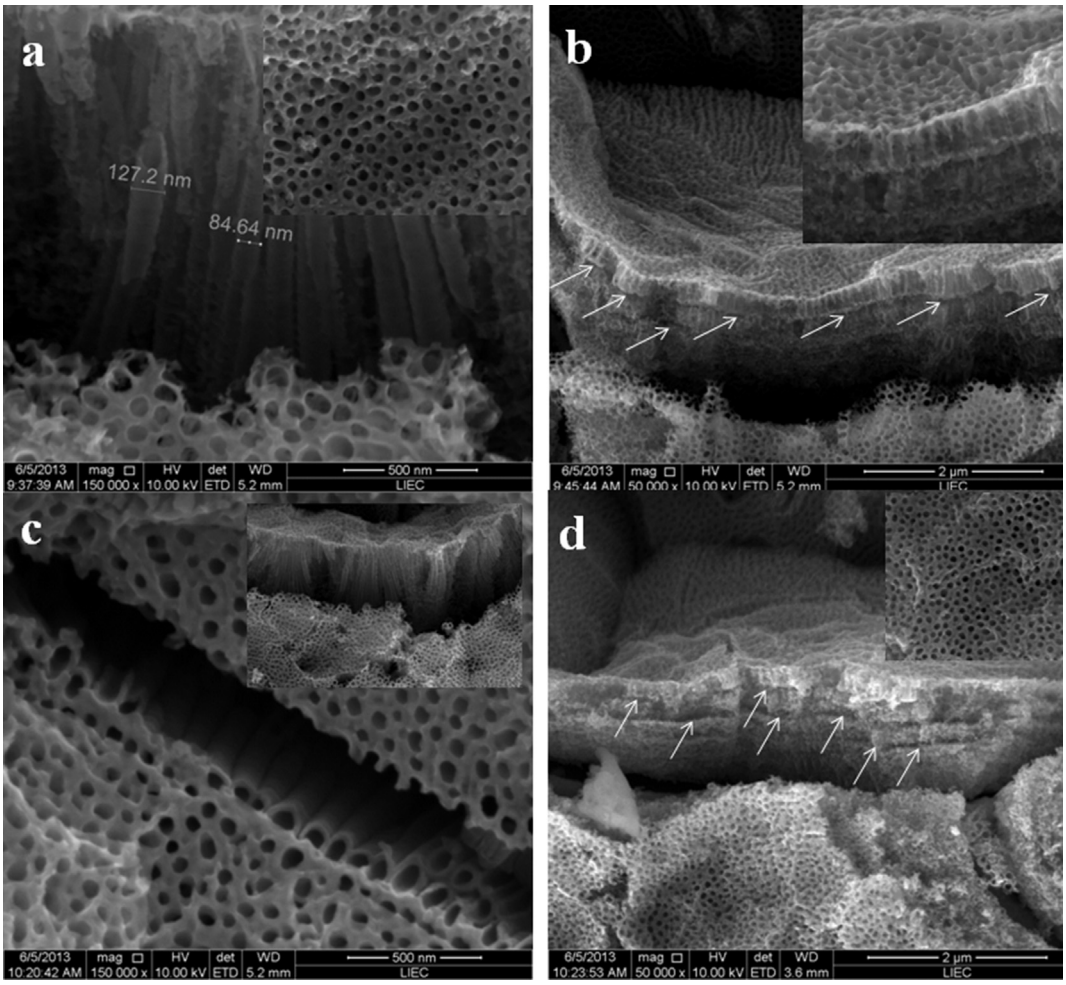

Fig. 6 – FESEM images showing TiO_2NTs grown under different anodization conditions. a) TiO_2NT under constant voltage, b) TiO_2NT under pulsed voltage, c) TiO_2NT/ZnS_{QDs} under constant voltage d) TiO_2NT/ZnS_{QDs} under pulsed voltage.

Table 1 – Structural parameters obtained using Rietveld refinement for TiO_2NT-CV, TiO_2NT-PV, TiO_2NT-ZnS-CV and TiO_2NT-ZnS-PV photoelectrodes.

Sample	a = b (Å)	c (Å)	χ^2	R (F**2)	wRp	Rp
TiO_2NT-CV	3.78728	9.495975	1.299	0.1736	0.1799	0.1339
TiO_2NT-PV	3.787715	9.497262	1.273	0.1908	0.1822	0.1385
TiO_2NT-ZnS-CV	3.78587	9.50039	1.142	0.2662	0.1840	0.1383
TiO_2NT-ZnS-PV	3.788046	9.494855	1.177	0.2199	0.1850	0.1423

TiO_2 Anatase – ICSD-202242 space group I 41/a m d Z (141) Tetragonal a = b = 3.78479 Å, c = 9,51237 Å, α = β = γ = 90°, V = 136.3 Å.

$$Z(\omega) = \left(\frac{R_{tr}R_{ct}}{1+i\omega/\omega_{rec}}\right)^{1/2} \coth\left[\left(\frac{R_{tr}}{R_{ct}}\right)^{1/2}\left(1+\frac{i\omega}{\omega_{rec}}\right)^{1/2}\right] \quad (1)$$

Here, R_{tr} is the total transport resistance, R_{ct} is the charge transfer resistance at the solid/electrolyte interface along the resistive transport channel, ω_{rec} is the radian frequency of the charge-transfer process, $\omega_{rec} = (R_{ct}C_{dl})^{-1}$, related to electron lifetime [35] by $\tau = \omega_{rec}^{-1}\, C_{dl}$. C_{dl}, is the total capacitance in the solid phase and solid-electrolyte interface related to the double layer. C_{dl} has several possible contributions [36]: i) the chemical capacitance of the semiconductor, C_μ, ii) the depletion capacitance at the semiconductor surface, C_{dpl} and iii) the Helmholtz capacitance of the surface, C_H. Total film capacitance has an additional capacitance from the exposed surface of the barrier layer at the bottom of the nanotubes.

In the case of low reactivity for electron transport, given by the condition $R_{ct} > R_{tr}$ [33], for frequencies higher than $\omega_1 = (R_{tr}C_{dl})^{-1}$, Eq. (1) reduces to:

$$Z = \left(\frac{R_{tr}}{C_{dl}}\right)^{1/2} (i\omega)^{-1/2} \quad (2)$$

Equation (2) is often termed the "Warburg" impedance, appearing as a straight line in the complex impedance plot in

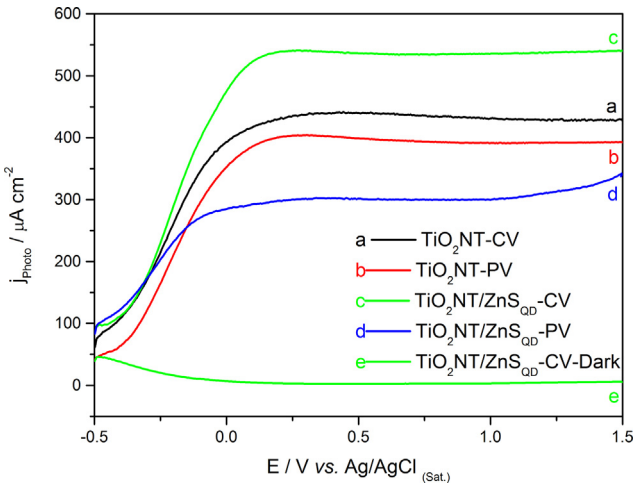

Fig. 7 – Linear sweep voltammogram for TiO_2NT and TiO_2NT/ZnS_{QDs} obtained in 0.5 M Na_2SO_4. 100 μW cm^{-2} Xenon lamp and 1.5G. v = 50 mV s^{-1}. T = 25 °C.

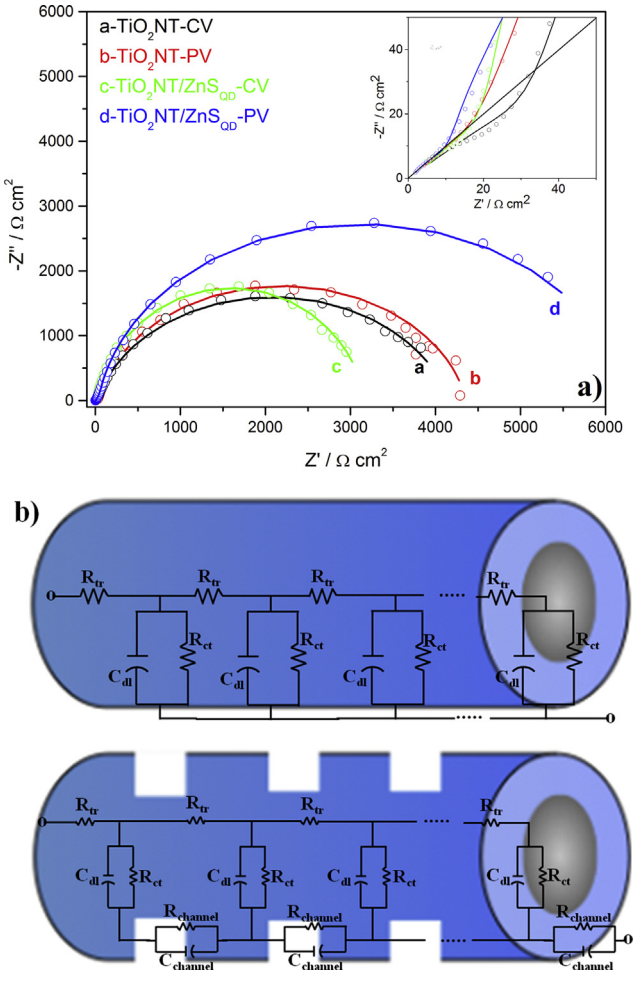

Fig. 8 – a) Nyquist spectra for TiO_2NT and TiO_2NT/ZnS_{QDs} under illumination in 0.5 M Na_2SO_4. E = 0.2 V. T = 25 °C. Inset: high frequency domain for TiO_2NT and TiO_2NT/ZnS_{QDs}. b) Transmission line representation of the i) TiO_2NT and ii) TiO_2NT/ZnSQDs.

the high frequency region in Fig. 8a (inset). It should be stressed that, in contrast to semi-infinite diffusion, in the TL model the 45° characteristic appears only in the high-frequency part of the impedance spectrum. As the frequency decreases, the charge-transfer resistance gives rise to a semicircle at low frequencies, consisting of the parallel combination of R_{ct} and C_{dl}, as shown in Fig. 8a.

In this sense, the TL model required to IS physical description data for the smooth morphology of TiO_2NT consisted of a simple double-channel TL, which is presented in Fig. 8b. In this model, both TiO_2NT and ions in the pore solution are described by Ohm's law and the interface with capacitance and resistance in parallel. In such a model, the transport resistance (R_{tr}) is associated in series with the double layer capacitance (C_{dl}) and charge transfer resistance (R_{ct}) associated in parallel. Therefore, using the model described above for both TiO_2NT-CV and TiO_2NT/ZnS_{QD}-CV, an excellent fit was obtained, meaning that the *Chi-square* values between the experimental and fitted data were 0.9997 and 0.9998, respectively. The proposed model is in agreement with the F-test [37].

Although both TiO_2NT-CV and TiO_2NT/ZnS_{QD}-CV exhibited a smooth morphology, the R_{tr} values obtained for TiO_2NT/ZnS_{QD}-CV were lower (15.8 Ω cm^{-1}) than for the TiO_2NT-CV (32.5 Ω cm^{-1}) photoanodes, which could be explained by QDs dispersion over the nanotube surface. Additionally, a decrease in the R_{ct} value was observed for the TiO_2NT/ZnS_{QD}-CV photoanode (3345 Ω cm^{-1}) compared to the TiO_2NT-CV (4336 Ω cm^{-1}) photoanode. These results could explain the high mobility as well as low recombination, which were inferred from the results presented in Fig. 7 and the morphologies presented in Fig. 6. These results are summarized in Table 2.

Bisquert et al. studied TiO_2 nanofibers [32] and TiO_2 nanotubes [6] for quantum dot solar cells and DSSC applications, respectively. Over such TiO_2 nanostructures, Bisquert et al. [6,32] proposed a similar TL model, which we used in this work. Moreover, when studying conducting polymer films, Bisquert et al. [8] observed the same TL model described above and, according to the authors [8], such TL model can be directly interpreted in terms of the transport and reaction processes occurring in the film.

TiO_2NT obtained at constant and pulsed voltage were significantly different, not just in terms of their morphologies, but also in the TL description required. In the pulsed voltage samples, the model consists of a simple double-channel TL, which is presented in Fig. 8b. In this model, both TiO_2NT and ions in the pore solution are described by Ohm's law and the

Table 2 – Fit quality, transport, charge transfer and channel resistance for TiO_2NT-CV, TiO_2NT-PV, TiO_2NT-ZnS-CV and TiO_2NT-ZnS-PV photoelectrodes.

Electrode	χ^2	R_{tr}/Ω cm^{-1}	R_{ct}/Ω cm^{-1}	$R_{Channel}$/ Ω cm^{-1}
TiO_2NT-CV	0.9997	32.5	4336	–
TiO_2NT-PV	0.9993	86.5	4144.5	45.5
TiO_2NT/ZnS_{QD}-CV	0.9998	15.8	3345	–
TiO_2NT/ZnS_{QD}-PV	0.9995	90.7	6203.3	85.2

interface with capacitance and resistance in parallel. However, in the present case, it was necessary to improve the TL model with additional electric equivalent elements to reflect the anisotropic channels due to the rippled morphology. In such model, transport resistance (R_{tr}) is associated in series with the double layer capacitance (C_{dl}) and charge transfer resistance (R_{ct}) is associated in parallel. Finally, $R_{channel}$ (channel resistance) and $C_{channel}$ (channel capacitance) were added to improve the quality of fit. Using the model described above for both TiO_2NT-PV and TiO_2NT/ZnS_{QD}-PV, we obtained an excellent fit, meaning that the *Chi-square* values between the experimental data and fitteddatawere0.9993 and 0.9995, respectively, in agreement with the *F*-test [37].

Although both TiO_2NT-PV and TiO_2NT/ZnS_{QD}-PV possessed a rippled morphology, the R_{tr} values obtained for TiO_2NT/ZnS_{QD}-PV and TiO_2NT-PV were similar: 90.7 Ω cm^{-1} and 86.5 Ω cm^{-1}. The R_{ct} obtained for TiO_2NT/ZnS_{QD}-PV (6203.3 Ω cm^{-1}) was higher than for the TiO_2NT-PV (4144.5 Ω cm^{-1}) photoanode. Therefore, by analyzing the data from a transport resistance point of view, the morphology is more important than the presence of ZnS quantum dots. Otherwise, the charge transfer resistance is strongly dependent of the presence of ZnS quantum dots. Finally, it was possible to observe that the $R_{channel}$ value obtained for TiO_2NT/ZnS_{QD}-PV (85.2 Ω cm^{-1}) was greater than that from the TiO_2NT-PV (45.5 Ω cm^{-1}) photoanode. The results are summarized in Table 2.

Sargent et al. [38] studied PbS_{QDs} deposited onto smooth and irregular surfaces. According to the authors [38], the external quantum efficiency increased by 476% for PbS_{QDs} deposited onto a smooth surface, along with increases in transport and charge separation. Li et al. [39] and Arakawa et al. [40] studied the deposition of CdS/CdSe QDs over ZnO [39] and InAs/GaAs [40] QDs, respectively. The authors [39,40] observed that there was a maximum in the thickness [39] and staking number of nanostructure layers [40] over QDs deposited for photo-device applications. Consequently, increasing the roughness led to a decrease in the photoconversion efficiency of QDs deposited onto a rippled morphology, since QDs are prone to clustering in the crevices formed by pulsed voltage anodization, as observed in the present study. It is well observed as described in Fig. 7, where is it possible to notice higher current density values for TiO_2NT-PV compared to TiO_2NT/ZnS_{QDs}-PV.

From a different point of view, the decreasing in the photoactivity of rippled TiO_2NT morphologies for the water splitting reaction can be analyzed considering strain in the sample [41–43]. The presence of strain reduces the crystal symmetry and modifies the energy band lineup. Moreover, such a strained heterostructure surface exhibits a chemical interface gradient spread over the surface [43]; it is known that the performance of surface devices is influenced by the quality of the interface [44]. In fact, interface crystalline imperfections such as planarity and composition gradients [45] cause scattering processes, leading to a reduction in the exciton decay time [46], a limitation in electron mobility [47] and an increase in non-radiative recombination [48]. As a result, superior photoelectrochemical activity was observed in this study for TiO_2NT after constant voltage anodization, as this technique led to a smooth morphology for the water splitting reaction.

In a common description, charge transport occurs due to electrostatic force-induced drift and the transport associated with the spatial charge gradient. However, in the case of disordered systems, it is known that mobility does not have a defined value [49]; in other words, transport is determined by a broad distribution of mobility due to the random nature of charge carrier transport in an energetically and spatially disordered environment. As consequence, there is a relaxation of the charge carrier process as a function of time [49], leading to an inhomogeneous distribution of transport properties throughout the film [50]. A detailed experimental investigation of the relationship between the macroscopic behavior and the microscopic transport statistic, however, requires the extraction of the transport parameter distribution, which can be modeled by an envelope function:

$$f(x) = y_0 + \frac{A}{t_0} e^{\frac{1}{2}\left(\frac{w}{t_0}\right)^2} e^{-\frac{x-x_0}{t_0}} \int_{-\infty}^{z} \frac{1}{\sqrt{2\pi}} e^{-\frac{y^2}{2}} dy \quad (3)$$

where,

$$z = \frac{x - x_c}{w} - \frac{w}{t_0} \quad (4)$$

y_0, A, x_c and w are the offset, area, center and width of this Gaussian function, respectively. At this point, we must stress out the importance of t_0. This variable is necessary to describe the asymmetric Gaussian tail. In this sense, it is possible to model the photocurrent spectrum, as observed in Fig. 9, and correlate it with the t_0 parameter. Therefore, as t_0 values increase, the asymmetric Gaussian tail becomes larger. Consequently, the charge carrier transport and recombination processes have abroad energy range and inhomogeneity.

A unifying theme in nanoscience is that the size and shape of nanostructures are important. Therefore, by analyzing the envelope function proposed above, it is possible to understand

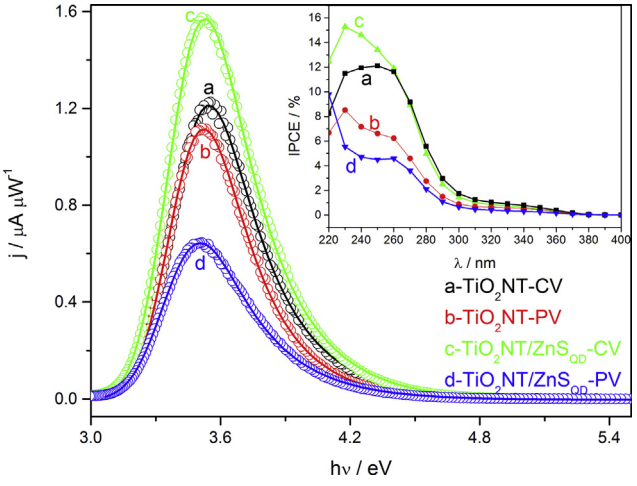

Fig. 9 – Photocurrent spectra for TiO_2NT and TiO_2NT/ZnS_{QDs} under constant and pulsed voltage anodization in 0.5 M Na_2SO_4. T = 25 °C. Inset: IPCE spectra for TiO_2NT and TiO_2NT/ZnS_{QDs}.

and to compare nanomaterials regarding the implications of the size-tunable properties of excitons. The t_0 and coefficient of determination (χ^2) [51] values obtained for TiO_2NT-CV, TiO_2NT-PV, TiO_2NT/ZnS_{QD}-CV and TiO_2NT/ZnS_{QD}-PV are presented in Table 3.

In summary, the pulsed voltage process resulted in large t_0 values because of the higher density of induced symmetry discontinuity along the nanotubes. Drabold et al. [52] studied amorphous and crystalline TiO_2 regarding its structural, electronic and optical properties using theoretical methods such as density functional theory (DFT). According to the authors [52], the tail states near the band edges are localized in amorphous TiO_2in contrast to crystalline TiO_2. The authors concluded [52] that the valence tail states result from the positional disorder of O atoms, whereas the conduction tail states result from over-coordinated Ti atoms. Therefore, the amorphous and crystalline TiO_2 structures exhibited differences in tail states. Hutchison et al. [53] studied potential energy distributions of organic molecules on several substrates, and observed asymmetric Gaussian distributions by Kelvin probe force microscopy (KPFM) and dynamic Monte Carlo simulations. According to the authors [53], with a distribution of spatially heterogeneous traps (e.g., positive charges) and more homogeneous opposing charges, the simulated histograms of surface potentials show a clear asymmetric skew, much like the experimental KPFM results. In general, both experimental and simulated skewed peaks fit poorly to either Gaussian or Lorentzian profiles, but fit well to a Voigt profile, representing a convolution of homogeneous (Lorentzian) and inhomogeneous (Gaussian) disorder. The authors concluded that, if the asymmetry in potential distributions was indeed caused by spatially heterogeneous disorder and trapped charges within the film, substrate, and/or interface, a Gaussian distribution would not always be an accurate model for disorder in devices made of these materials. Therefore, as proposed herein, we suggest an envelope function composed by a Gaussian and exponential profile able to adjust experimental data and correlate them with anisotropy and morphology.

The proposition to build nanotubes envisages enhancing the overall photoconversion efficiency by decreasing the trapping-detrapping process [54]. Thus, it is expected that synthesizing anisotropic photoelectrocatalysts such as the nanotubes obtained under pulsed voltage conditions, in general, will decrease photoconversion efficiency [54]. These facts could explain the data in Fig. 9 (inset), where it can be observed that the IPCE values increased by 210% for TiO_2NT/ZnS_{QD}-CV compared to TiO_2NT/ZnS_{QD}-PV at 240 nm. Using hollow TiO_2 nanofiber in a DSSC system, Bisquert et al. [54] obtained IPCE values close to 10%. Matsuda et al. [55] studied the water splitting reaction over TiO_2NT prepared under similar conditions described herein and observed IPCE values up to 18%.

Table 3 – Fit quality and asymmetric Gaussian tail parameters obtained for TiO_2NT-CV, TiO_2NT-PV, TiO_2NT-ZnS-CV and TiO_2NT-ZnS-PV photoelectrodes.

Electrode	χ^2	t_0
TiO_2NT-CV	0.99968	0.219
TiO_2NT-PV	0.99972	0.243
TiO_2NT/ZnS_{QD}-CV	0.99962	0.250
TiO_2NT/ZnS_{QD}-PV	0.99946	0.265

To increase TiO_2 visible light absorption, doping [56], sensitization with small bandgap semiconductors [57–59] or combination of doping and sensitization [60] are nowadays seriously investigated. Focusing on sensitization approach, combining TiO_2 with narrow bandgaps II–VI quantum dots, such as ZnS, CdS, CdSe, or CdTe, appears particularly promising. Indeed, such QD nanocrystals exhibit *i*) exceptional photo absorption properties which can be tuned from IR to UV ranges by varying their average size, *ii*) an excellent photostability, and *iii*) a high quantum yield [61]. Here it is possible to observe that TiO_2NT-CV have lower bandgap energy when compared with TiO_2NT-PV and reduces even further when the nanotubes was decorates with ZnS. The exponential optical absorption edge and hence the optical band gap are controlled by the morphology and degree of structural order disorder on the TiO_2NTlattices strain [62,63]. The decrease in the band gap can be directly relates to the morphology and defects in the TiO_2NT lattice.

In TiO_2 and ZnS, the material properties are primarily associated with the cluster constituents. The disparity or mismatch of, which can be generated by breaking the symmetry process of these clusters, such as cluster distortions or displacements [14,64], can induce structural order-disorder effects, which will significantly influence the electrical properties. Breathings and tilts create a large number of different structures and subsequently different photocatalysts.

The transfer process between clusters in the lattice of TiO_2 or ZnS crystals can be attributed to order-disorder effects among clusters, and this process can promote charge transfer. The cluster-to-cluster charge transfer (CCCT) [65] in a crystal containing more than one kind of cluster is characterized by electronic transitions and recombination processes from one cluster to another cluster, according to the following equations:

$$[TiO_6]^x + [TiO_5V_O^x] \rightarrow [TiO_6]^{'} + [TiO_5V_O^{\cdot}] \quad (5)$$

$$2[TiO_5V_O^{\cdot}] + 2H_2O \rightarrow 2[TiO_5V_O^x] + 2OH^* + 2H^{\cdot} \quad (6)$$

$$2OH^* \rightarrow O_2 + 2H^{\cdot} \quad (7)$$

$$2[TiO_6]^{'} + 4H^{\cdot} \rightarrow 2[TiO_6]^x + 2H_2 \quad (8)$$

where $[TiO_6]^x$ clusters are neutral and receptor of electrons, $[TiO_5V_O^x]$ clusters are also neutral but donate of electrons. When occurs the CCCT, the $[TiO_6]^x$ and $[TiO_5V_O^x]$ clusters forming the $[TiO_6]^{'}$ and $[TiO_5V_O^{\cdot}]$ that are singly ionized states and donate and capture electrons, respectively.

Equations (5)–(8) are valid for pure TiO_2 nanotubes. When nanotubes are decorated with ZnS nanoparticles, there is an interaction between the semiconductors. This interaction can generate a known density of e^-/h^+, which will enhance the water decomposition process or produce the annihilation of e^-/h^+. In the case of the TiO_2NT/ZnS_{QD}-CV samples, there was a synergy in the H_2O decomposition process, unlike the case of the TiO_2NT/ZnS_{QD}-PV samples, as shown in Fig. 10a and b, respectively.

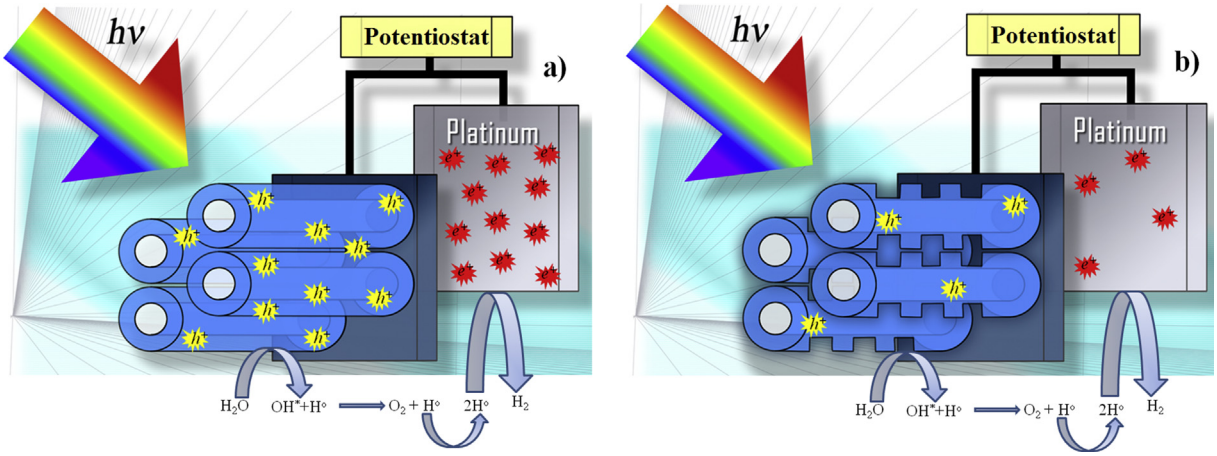

Fig. 10 – Schematic presentation of the proposed water splitting reaction model over a) constant and b) pulsed voltage anodization.

The equation for the ZnS nanoparticles are similar to the TiO_2, for the action of $[ZnS_4]^x$ and $[ZnS_3V_S^x]$ clusters.

The results presented above demonstrates using theoretical calculus and experimental data, that TiO_2NT synthesized using constant voltage anodization lead to an enhancement in the water splitting photoactivity due to smoother surface. Although the atomic and electronic structures of the charge-trapping defects lack clear understanding, it was demonstrated above that induced anisotropic morphologies are prone to exhibiting charge-trapping sites with both shallow and deep traps.

Conclusions

In summary, TiO_2NT array photoelectrodes prepared under constant or pulsed applied voltage resulted in smooth and rippled nanotube morphologies. The microwave-assisted solvothermal method was useful to deposit ZnS nanoparticles along the TiO_2NTs with distinct morphologies. It was possible to tune the electronic and structural properties of these ZnS nanoparticles, which led to an increase in the photoelectrochemical water splitting reaction. An agreement was obtained between the proposed envelope function and the inhomogeneous distribution of transport properties throughout the smooth and rippled morphologies. Anisotropic morphology tended to exhibit charge trapping sites with shallow and deep traps, since the photocurrent observed for the water splitting reaction increased by 80% for the TiO_2NT/ZnS_{QD}-CV photoelectrode compared to the TiO_2NT/ZnS_{QD}-PV photoelectrode. Finally, significant differences between smooth and rippled TiO_2 nanotubes were modeled using transmission line and impedance spectroscopy.

Compliance with ethical standards

This study was funded by CNPq, CAPES and FAPEMAT.

Acknowledgments

The authors would like to thank the Brazilian research funding institutions CNPq (427161/2016-9), CAPES, FAPESP (2010/05555-2, 2012/06778-0, 2012/22823-6) and FAPEMAT (214599/2015) for financial support and M. M. P. Machado for the schematic art and figures. R. G. Freitas is grateful to CENAPAD/SP (Proj650) for providing computational time.

Appendix A. Supplementary data

Supplementary data related to this article can be found at https://doi.org/10.1016/j.ijhydene.2018.02.113.

REFERENCES

[1] van de Krol R, Grätzel M. Photoelectrochemical hydrogen production: emphasizes defect chemical aspects of metal oxide photoelectrodes. 1st ed. Springer; 2012.
[2] Macak JM, Tsuchiya H, Ghicov A, Yasuda K, Hahn R, Bauer S, et al. TiO_2 nanotubes: self-organized electrochemical formation, properties and applications. Curr Opin Solid State Mater Sci 2007;11:3–18.
[3] Albu SP, Kim D, Schmuki P. Growth of aligned TiO_2 bamboo-type nanotubes and highly ordered nanolace. Angew Chem Int Ed 2008;47:1916–9.
[4] Ji Y, Zhang M, Cui J, Lin K-C, Zheng H, Zhu J-J, et al. Highly-ordered TiO_2 nanotube arrays with double-walled and bamboo-type structures in dye-sensitized solar cells. Nano Energy 2012;1:796–804.
[5] Zhang Z, Hossain MF, Takahashi T. Photoelectrochemical water splitting on highly smooth and ordered TiO_2 nanotube arrays for hydrogen generation. Int J Hydrogen Energy 2010;35:8528–35.
[6] Fabregat-Santiago F, Barea EM, Bisquert J, Mor GK, Shankar K, Grimes CA. High carrier density and capacitance in TiO_2 nanotube arrays induced by electrochemical doping. J Am Chem Soc 2008;130:11312–6.

[7] Bisquert J, Garcia-Belmonte G, Fabregat-Santiago F, Compte A. Anomalous transport effects in the impedance of porous film electrodes. Electrochem Commun 1999;1:429–35.
[8] Bisquert J, Belmonte GG, Santiago FF, Ferriols NS, Yamashita M, Pereira EC. Application of a distributed impedance model in the analysis of conducting polymer films. Electrochem Commun 2000;2:601–5.
[9] Li Z-X, Xie Y-L, Xu H, Wang T-M, Xu Z-G, Zhang H-L. Expanding the photoresponse range of TiO_2 nanotube arrays by CdS/CdSe/ZnS quantum dots co-modification. J Photochem Photobiol A Chem 2011;224:25–30.
[10] Jun HK, Careem MA, Arof AK. Quantum dot-sensitized solar cells—perspective and recent developments: a review of Cd chalcogenide quantum dots as sensitizers. Renew Sustain Energy Rev 2013;22:148–67.
[11] Robel I, Kuno M, Kamat PV. Size-dependent electron injection from excited CdSe quantum dots into TiO_2 nanoparticles. J Am Chem Soc 2007;129:4136–7.
[12] Yu WW, Qu L, Guo W, Peng X. Experimental determination of the extinction coefficient of CdTe, CdSe, and CdS nanocrystals. Chem Mater 2003;15:2854–60.
[13] Vogel R, Hoyer P, Weller H. Quantum-sized PbS, CdS, Ag_2S, Sb_2S_3, and Bi_2S_3 particles as sensitizers for various nanoporous wide-bandgap semiconductors. J Phys Chem 1994;98:3183–8.
[14] de Santana YVB, Raubach CW, Ferrer MM, La Porta F, Sambrano JR, Longo VM, et al. Experimental and theoretical studies on the enhanced photoluminescence activity of zinc sulfide with a capping agent. J Appl Phys 2011;110:123507.
[15] Rietveld H. A profile refinement method for nuclear and magnetic structures. J Appl Crystallogr 1969;2:65–71.
[16] Larson AC, Von Dreele RB. General structure analysis system - GSAS, los alamos national laboratory report LAUR. 2004. p. 86–748.
[17] Toby B. EXPGUI, a graphical user interface for GSAS. J Appl Crystallogr 2001;34:210–3.
[18] Dovesi R, Saunders VR, Roetti C, Orlando R, Zicovich-Wilson CM, Pascale F, et al. CRYSTAL09 User's Manual. Torino; 2009.
[19] Becke AD. Density-functional thermochemistry. III. The role of exact exchange. J Chem Phys 1993;98:5648–52.
[20] Lee C, Yang W, Parr RG. Development of the Colle-Salvetti correlation-energy formula into a functional of the electron density. Phys Rev B 1988;37:785–9.
[21] http://www.tcm.phy.cam.ac.uk/~mdt26/crystal.html.
[22] Gatti C, Saunders VR, Roetti C. J Chem Phys 1994;101:10686.
[23] Kokalj A. Computer graphics and graphical user interfaces as tools in simulations of matter at the atomic scale. Comput Mater Sci 2003;28:155–68.
[24] Longo V, Cavalcante L, Costa MS, Moreira M, de Figueiredo A, Andrés J, et al. First principles calculations on the origin of violet-blue and green light photoluminescence emission in $SrZrO_3$ and $SrTiO_3$ perovskites. Theor Chem Acc 2009;124:385–94.
[25] Wood DL, Tauc J. Weak absorption tails in amorphous semiconductors. Phys Rev B 1972;5:3144–51.
[26] Macák JM, Tsuchiya H, Schmuki P. High-aspect-ratio TiO_2 nanotubes by anodization of titanium. Angew Chem Int Ed 2005;44:2100–2.
[27] Palmas S, Da Pozzo A, Delogu F, Mascia M, Vacca A, Guisbiers G. Characterization of TiO2 nanotubes obtained by electrochemical anodization in organic electrolytes. J Power Sources 2012;204:265–72.
[28] Bakhshayesh AM, Mohammadi MR, Fray DJ. Controlling electron transport rate and recombination process of TiO_2 dye-sensitized solar cells by design of double-layer films with different arrangement modes. Electrochim Acta 2012;78:384–91.
[29] de Levie R. On porous electrodes in electrolyte solutions. Electrochim Acta 1963;8:751–80.
[30] de Levie R. On porous electrodes in electrolyte solutions—IV. Electrochim Acta 1964;9:1231–45.
[31] De Levie R. The influence of surface roughness of solid electrodes on electrochemical measurements. Electrochim Acta 1965;10:113–30.
[32] Han H, Sudhagar P, Song T, Jeon Y, Mora-Sero I, Fabregat-Santiago F, et al. Three dimensional-TiO_2 nanotube array photoanode architectures assembled on a thin hollow nanofibrous backbone and their performance in quantum dot-sensitized solar cells. Chem Commun 2013;49:2810–2.
[33] Bisquert J, Garcia-Belmonte G, Fabregat-Santiago F, Ferriols NS, Bogdanoff P, Pereira EC. Doubling exponent models for the analysis of porous film electrodes by impedance. Relaxation of TiO_2 nanoporous in aqueous solution. J Phys Chem B 2000;104:2287–98.
[34] Bisquert J. Theory of the impedance of electron diffusion and recombination in a thin layer. J Phys Chem B 2002;106:325–33.
[35] Bisquert J, Zaban A, Greenshtein M, Mora-Seró I. Determination of rate constants for charge transfer and the distribution of semiconductor and electrolyte electronic energy levels in dye-sensitized solar cells by open-circuit photovoltage decay method. J Am Chem Soc 2004;126:13550–9.
[36] Bisquert J. Chemical capacitance of nanostructured semiconductors: its origin and significance for nanocomposite solar cells. Phys Chem Chem Phys 2003;5:5360–4.
[37] Orazem ME, Tribollet B. Electrochemical impedance spectroscopy. John Wiley & Sons; 2008.
[38] Klem EJD, MacNeil DD, Cyr PW, Levina L, Sargent EH. Efficient solution-processed infrared photovoltaic cells: planarized all-inorganic bulk heterojunction devices via inter-quantum-dot bridging during growth from solution. Appl Phys Lett 2007;90, 183113.
[39] Hou Q, Zhu L, Chen H, Liu H, Li W. Highly regular and ultra-thin porous ZnO nanosheets: an indirect electrodeposition method using acetate-containing precursor and their application in quantum dots-sensitized solar cells. Electrochim Acta 2013;94:72–9.
[40] Yang T, Tatebayashi J, Nishioka M, Arakawa Y. Effects of accumulated strain on the surface and optical properties of stacked 1.3 μm InAs/GaAs quantum dot structures. Phys E Low Dimens Syst Nanostruct 2008;40:2182–4.
[41] Osbourn GC. Strained-layer superlattices: a brief review. Quantum Electron IEEE J 1986;22:1677–81.
[42] Voisin P. Misfit strains in semiconductor superlattices. Surf Sci 1986;168:546–52.
[43] O'Reilly EP, Witchlow GP. Theory of the hole subband dispersion in strained and unstrained quantum wells. Phys Rev B 1986;34:6030–3.
[44] Hasegawa H, Akazawa M. Interface models and processing technologies for surface passivation and interface control in III–V semiconductor nanoelectronics. Appl Surf Sci 2008;254:8005–15.
[45] Grützmacher D. Growth and analysis of quantum well structures. J Cryst Growth 1991;107:520–30.
[46] Sun CQ. Size dependence of nanostructures: impact of bond order deficiency. Prog Solid State Chem 2007;35:1–159.
[47] Lima FMS, Veloso AB, Fonseca ALA, Nunes OAC, da Silva Jr EF. Variational results for electron mobility in modulation-doped $In_{0.53}Ga_{0.47}As/InP$ single symmetric quantum wells. Microelectron J 2005;36:1016–9.
[48] Miyazaki J, Kinoshita S, Jin T. Non-radiative exciton recombination through excitation energy transfer in quantum dot clusters. J Lumin 2011;131:539–42.

[49] Scher H, Montroll EW. Anomalous transit-time dispersion in amorphous solids. Phys Rev B 1975;12:2455–77.
[50] Bässler H. Charge transport in disordered organic photoconductors a Monte Carlo simulation study. Phys status Solidi B 1993;175:15–56.
[51] Box GEP, Hunter JS, Hunter WG. Statistics for experimenters: design, innovation, and discovery. 2005.
[52] Prasai B, Cai B, Underwood MK, Lewis J, Drabold DA. Properties of amorphous and crystalline titanium dioxide from first principles. J Mater Sci 2012;47:7515–21.
[53] Hoffmann PB, Gagorik AG, Chen X, Hutchison GR. Asymmetric surface potential energy distributions in organic electronic materials via Kelvin probe force microscopy. J Phys Chem C 2013;117:18367–74.
[54] Teoh WY, Scott JA, Amal R. Progress in heterogeneous photocatalysis: from classical radical chemistry to engineering nanomaterials and solar reactors. J Phys Chem Lett 2012;3:629–39.
[55] Krengvirat W, Sreekantan S, Noor A-FM, Kawamura G, Muto H, Matsuda A. Single-step growth of carbon and potassium-embedded TiO_2 nanotube arrays for efficient photoelectrochemical hydrogen generation. Electrochim Acta 2013;89:585–93.
[56] Asahi R, Morikawa T, Ohwaki T, Aoki K, Taga Y. Visible-light photocatalysis in nitrogen-doped titanium oxides. Science 2001;293:269–71.
[57] Banerjee S, Mohapatra SK, Das PP, Misra M. Synthesis of coupled semiconductor by filling 1D TiO_2 nanotubes with CdS. Chem Mater 2008;20:6784–91.
[58] Shen Q, Sato T, Hashimoto M, Chen C, Toyoda T. Photoacoustic and photoelectrochemical characterization of CdSe-sensitized TiO_2 electrodes composed of nanotubes and nanowires. Thin Solid Films 2006;499:299–305.
[59] Gao X-F, Li H-B, Sun W-T, Chen Q, Tang F-Q, Peng L-M. CdTe quantum dots-sensitized TiO_2 nanotube array photoelectrodes. J Phys Chem C 2009;113:7531–5.
[60] Hensel J, Wang G, Li Y, Zhang JZ. Synergistic effect of CdSe quantum dot sensitization and nitrogen doping of TiO_2 nanostructures for photoelectrochemical solar hydrogen generation. Nano Lett 2010;10:478–83.
[61] Louie A. Multimodality imaging probes: design and challenges. Chem Rev 2010;110:3146–95.
[62] Longo E, Orhan E, Pontes FM, Pinheiro CD, Leite ER, Varela JA, et al. Density functional theory calculation of the electronic structure of $Ba_{0.5}Sr_{0.5}TiO_3$ Photoluminescent properties and structural disorder. Phys Rev B 2004;69:125115.
[63] Anicete-Santos M, Orhan E, de Maurera MAMA, Simões LGP, Souza AG, Pizani PS, et al. Contribution of structural order-disorder to the green photoluminescence of $PbWO_4$. Phys Rev B 2007;75:165105.
[64] Raubach CW, De Santana YVB, Ferrer MM, Buzolin PGC, Sambrano JR, Longo E. Photocatalytic activity of semiconductor sulfide heterostructures. Dalton Trans 2013;42:11111–6.
[65] Cavalcante LS, Longo VM, Sczancoski JC, Almeida MAP, Batista AA, Varela JA, et al. Electronic structure, growth mechanism and photoluminescence of $CaWO_4$ crystals. CrystEngComm 2012;14:853–68.